Microfiber rotational dynamics in turbulence

Vlad Giurgiu[1], Giuseppe C.A. Caridi[1,*], Marco De Paoli[1,2] Alfredo Soldati[1,3]

1: Institute of Fluid Mechanics and Heat Transfer,TUWien,Austria
2:Physics of Fluids Group,University of Twente,The Netherlands
3: Polytechnic Department, University of Udine, Italy
*Corresponding author: giuseppe.caridi@tuwien.ac.at

Keywords: 3D time-resolved fiber reconstruction, Anisotropic particles, Rotation rate measurements.

ABSTRACT

We measure the effect of turbulence on spinning and tumbling rates of microfibers in wall-bounded turbulence. The measurements are performed in a turbulent water channel at Reτ 720. Fibres are 1.2 mm long and 10 m in diameter (aspect ratio 120). Their length ranges from 4 to 12 Kolmogorov length scales. They are neutrally buoyant, inertial-less, and rigid in these flow conditions. Six high-speed cameras image the fibres at the channel centre and in a near-wall region. We employ and further refine a technique of tomographic fibre reconstruction and tracking. Their curved shape is used to define a fibre-fixed reference frame and measure its time-resolved orientation. Thus measurements of tumbling and spinning rates are enabled. We provide a discussion about the uncertainty on the rotation rates based on their shape and angular displacement between time-steps. Based on converged statistics, we observed that the mean and mean square spinning are higher than tumbling rates at both channel centre and near-wall region. In addition, our study reveals that slender, curved fibres behave akin to straight rods, yet their curved shape provides a unique advantage: this curvature allows us to measure all rotational components.

1. Introduction

Turbulent flows with suspended small anisotropic particles of non-spherical shape are a common occurrence in many industrial (e.g. papermaking, pharmaceutical processing, soot emission) and natural processes (e.g. pollen species, icy clouds, and plankton and marine snow). The fundamental problem of the dynamics of such small anisotropic particles is now a major obstacle to accurate determination of the fate of microplastics distribution in the oceans, freshwaters and in the atmosphere. Such microplastics scale with the smallest turbulence scales that control their dynamics, and although we have an understanding of the turbulence phenomena at these scales, we cannot currently predict the drag on non-spherical particles. Remain therefore beyond current modelling possibilities the settling and dispersion of microplastics in the environment [Voth & Soldati (2017)]. Moreover, numerical [Byron et al. (2015); Zhao et al. (2015); Marchioli & Soldati (2013); Marchioli et al. (2016); Yang et al. (2018)] and experimental [Parsa et al. (2012); Baker & Coletti (2022); Shaik

& van Hout (2023); Hoseini et al. (2015)] data on rotation rates are currently limited to anisotropic particles with aspect ratios ranging from 0.1 (oblate) to 100 (prolate ellipsoids) [Voth & Soldati (2017)]. Experiments by Ref.Alipour et al. (2021, 2022); Kuperman et al. (2019) report only tumbling rates of slender, curved fibres at the Kolmogorov length scale. However, the complete rotation rate of these particles remained unknown. Our study fills this gap by leveraging the curved shape to uniquely identify fibre orientation. We measure and distinguish between all rotation rate components, spinning and two tumbling rates in turbulent channel flow.

2. Methodology

Our experiments were done in the TU Wien Turbulent Water Channel. This facility, about 10 meters long, recirculates 3000 liters of water from the upstream reservoir to the test section and back. The inner cross-section, having a width-to-height aspect ratio of 10, minimises side-wall influence on mid-span measurements. 6 high-speed cameras placed above the channel and 1 high-power laser illuminating a volume about this size are used in this study. We've validated the flow characteristics of this facility against direct numerical simulations and found good agreement on velocity statistics up to 4th order. However, only the mean streamwise velocity over wall-normal coordinate in wall units is shown here. Our fiber-laden experiments are conducted at a Shear Reynolds number of 720, exploring two wall-normal regions: near-wall, where turbulent fluctuations and mean shear are dominant, and channel center, where turbulence is nearly isotropic and homogeneous. The details of the experimental setup are summerized in figure .
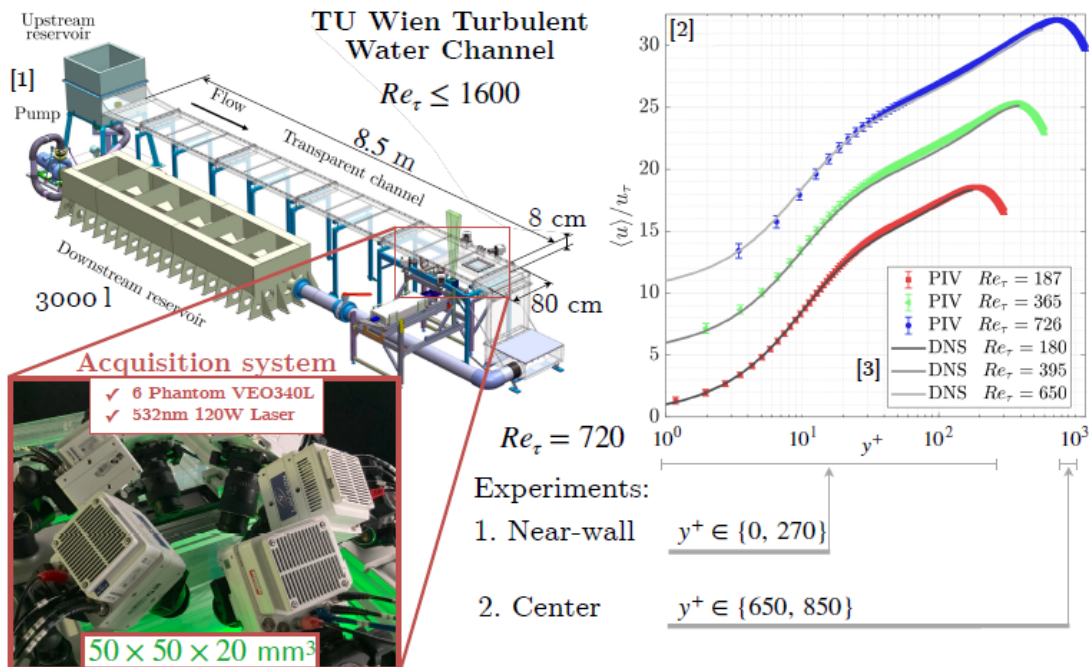

Figure 1. 1) Drawing of the experimental set-up with test section and imaging system. 2) Velocity profiles

The fibres are tracked using images from six high speed cameras in the TU Wien Turbulent Water

Channel, which produces statistically steady turbulent channel flow Giurgiu et al. (2023). The experiments are performed at a Shear Reynolds number, $Re_\tau = u_\tau h/\nu = 720$ at two wall-normal locations, $y^+ = y/\delta_\nu < 290$ and $y^+ > 630$. The working fluid is water at 15.2 with density $\rho = 1$ g cm^{-3} and viscosity $\nu = 1.13$ mm^2 s^{-1}.

The friction velocity ($u_\tau = \sqrt{\tau_w/\rho}$), viscous length ($\delta_\nu = \nu/u_\tau$) and time ($\tau = \delta_\nu/u_\tau$) scales are $u_\tau = 20.5$, $\delta_\nu = 55$, and $\tau = 2.7$. The Kolmogorov length ($\eta = (\nu^3/\epsilon)^{1/4}$) and time scale ($\tau_\eta = (\nu/\epsilon)^{1/2}$) range from the wall to channel centre $\eta = 83 - 292$ and $\tau_\eta = 5.7 - 75$. These values have been found by interpolating between the values obtained with DNS at $Re_\tau = 590$ Moser et al. (1999) and $Re_\tau = 950$ [Del Alamo et al. (2004)]. A method described in detail in Alipour et al. (2021)
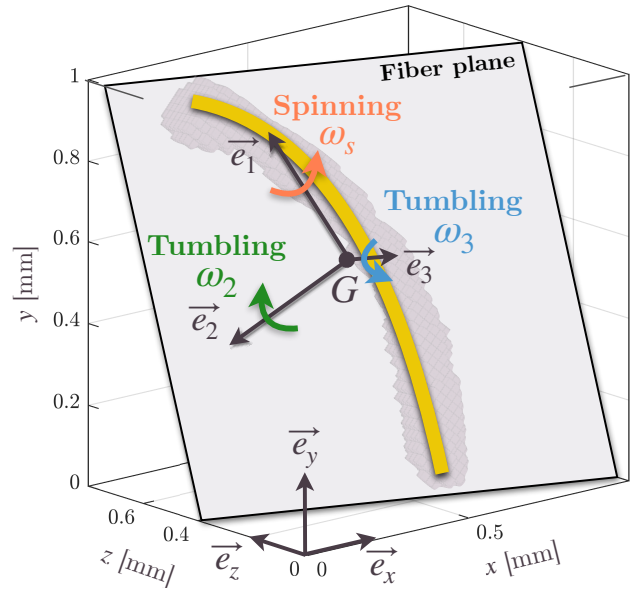

Figure 2. A reconstructed fibre (gray voxels) with its equivalent polynomial (yellow line), fixed coordinate system ($\vec{e_1}$, $\vec{e_2}$, $\vec{e_3}$) and center of mass G (black dot) are shown. The laboratory reference frame is $\vec{e_x}$ (stream-wise), $\vec{e_y}$ (wall-normal), and $\vec{e_z}$ (span-wise).

was used to reconstruct and track each fibre from the six 2D images. These measurements were improved with respect to Alipour et al. (2021, 2022) through the addition of two extra viewing directions, which increase the reconstruction accuracy [Giurgiu et al. (2023); Elsinga et al. (2006)] and by doubling the resolution, which reduces the orientation uncertainty [Caridi et al. (2023)]. The tomographic reconstruction of one fibre (resolution 49 vox$/mm$) is shown in Fig. 2. The object was replaced by a 2nd order polynomial (yellow line). The polynomials centre of mass (G) and the eigenvectors ($\vec{e_1}$, $\vec{e_2}$, $\vec{e_3}$ - in order of ascending eigenvalues) of its inertia tensor were measured. This unique identification of the fibre orientation is made possible by its curvature. The inset of Fig. 4 shows the the probability density function (pdf) of curvatures κ scaled by the equivalent curvature $\kappa_0 = 2.62$ of an arc of half a circle with the nominal fibre length. For straight fibres κ/κ_0 is 0.

The components of the eigenvectors are filtered using a Robust Locally Weighted Scatterplot Smoothing ('rlowess') [Cleveland (1979)] filter used also by Shaik & van Hout (2023); Shaik et al. (2020)

for reducing noise and removing outliers. Following Baker & Coletti (2022) we choose 15τ as the filter kernel width. We build the rotation matrix $R = (\vec{e_1}\ \vec{e_2}\ \vec{e_3})$. Its time derivative $\dot{R}$ is computed with first-order finite differences between time-steps $0.33\tau_\eta(y^+ = 720)$ apart. The skew-symmetric angular velocity matrix in the fibre fixed reference frame $(\vec{e_1}, \vec{e_2}, \vec{e_3})$ is $\Omega = R^{-1}\dot{R}$ [Lynch & Park (2017)]. Spinning is a rotation around $\vec{e_1}$ and tumbling around $\vec{e_2}$ and $\vec{e_3}$. Spinning and tumbling rates are $\omega_s = \Omega_{32}$, $\omega_2 = \Omega_{31}$, $\omega_3 = \Omega_{21}$, and $\omega_t = (\omega_2^2 + \omega_3^2)^{1/2}$, respectively.
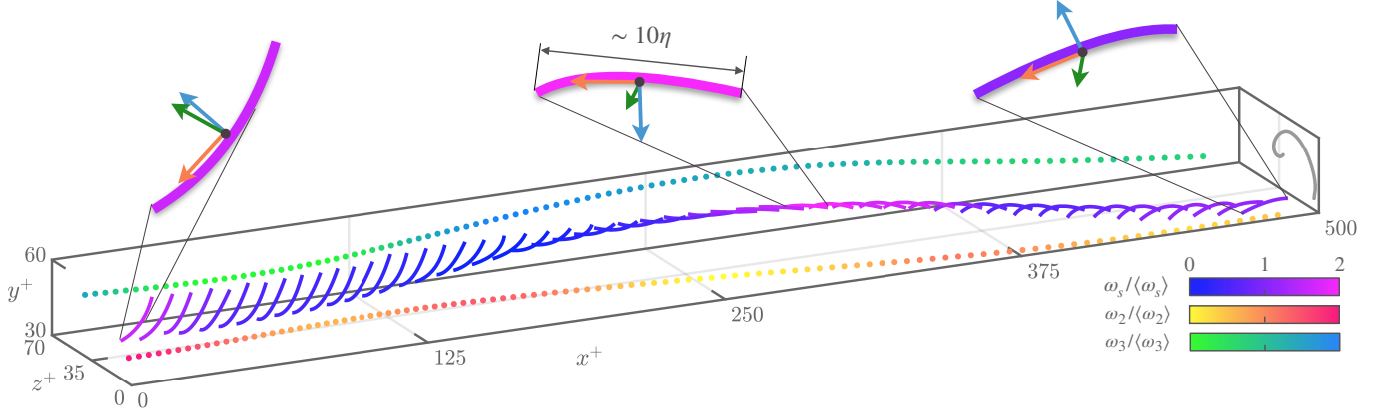

Figure 3. Three-dimensional view of a reconstructed fibre trajectory projected onto planes xz (coloured by ω_2), xy (coloured by ω_3), and equivalent polynomial (coloured by ω_s). Trajectory projection onto yz (grey line). The first, intermediate, and last instance of the fibre are magnified and shown above the main panel. The orange, green, and blue vectors represent the fibre fixed reference frame.

3. Rotational Rate

To investigate the impact of proximity to the channel wall, we examine tumbling rates scaled by the viscous time-scale over the wall-normal coordinate (see figure5(a)). To make comparisons, we rescale reference values from Kolmogorov to the viscous time scale, adjusting for our specific channel conditions. At the channel center, we observe a reduction in tumbling rates compared to rods in HIT conditions (point to black open square and cross Parsa & Voth and Ohemke). However, we note an increase compared to rods of higher inertia (point to black open diamond Baker & Coletti). Our measured profile, represented by purple diamonds, exhibits a qualitative similarity to rods in a turbulent boundary layer but with a noticeable shift to higher rates. Moreover, we find no significant difference between the individual tumbling components.

Turning our attention to spinning rates (5(b)), we've measured their evolution with the wall normal coordinate. Notably, at the channel center, our measured rates are in good agreement with rods HIT. Spinning rates are found to consistently surpass tumbling rates, both near the channel center and the wall. Finally, we've observed a qualitative similarity in the behaviour of spinning rates to tumbling rates near the wall, with a notable peak at 40 y plus.
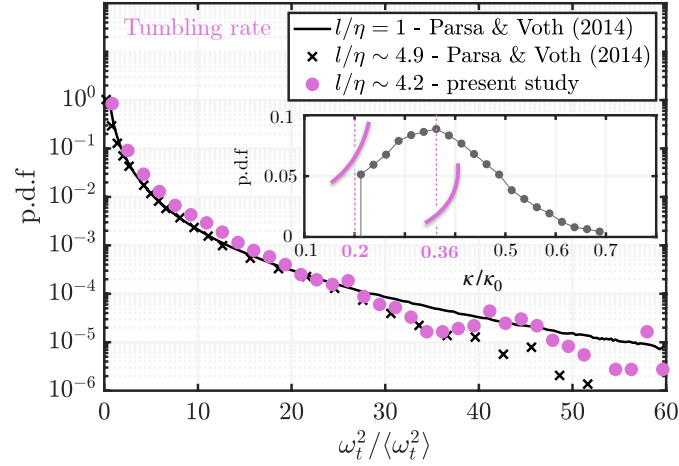
Figure 4. Main panel shows the p.d.f. of normalised tumbling rate (purple closed circle) compared to straight rods of $l/\eta = 1$ (black line) and $l/\eta \sim 4.9$ from Ref.Parsa & Voth (2014). The inset shows the p.d.f. of dimensionless curvature. Two example fibres (purple line) with curvatures of 0.2 and 0.36. to do: errorbars like Parsa and Voth and add their errorbars; update comments
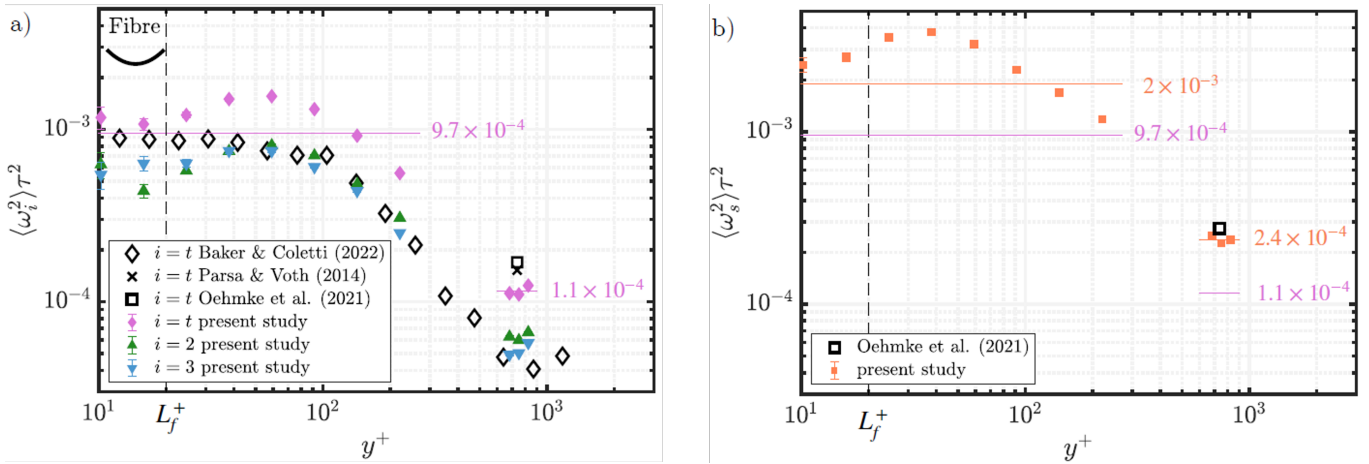
Figure 5. Mean square rotation rates normalised by the viscous time-scale as a function of wall-normal coordinate. (a) Second (upward pointing green triangle) and third component of tumbling (downward pointing blue triangle). Combined tumbling of present study (purple closed diamond) and by Baker and Coletti Baker & Coletti (2022) of straight rods in a turbulent boundary layer at $Re_\tau = 620$ and $St \sim \mathcal{O}(1)$. Purple lines indicate the mean tumbling for each experiment. Tumbling measurements of straight rods in HIT are shown in the channel centre: open black square, $l/\eta \sim 4.9$ from Ref.Parsa & Voth (2014) and black cross, $l/\eta \sim 11$ from Ref.Oehmke et al. (2021). (b) Measured spinning (closed orange square) and spinning of straight rods in HIT from Ref.Oehmke et al. (2021) ($l/\eta \sim 11$). Orange lines are mean spinning over the respective experiment. Tumbling mean from panel (a) is shown as purple lines. In both panels the vertical black dashed line indicates fibre length in wall units, L_f^+. still have to think about improvements on this figure

4. Conclusion

In summary, our study reveals that slender, curved fibres behave akin to straight rods, yet their curved shape provides a unique advantage: this curvature allows us to measure all rotational components. Our results are consistent with findings from both homogeneous isotropic turbulence studies Parsa & Voth (2014); Oehmke et al. (2021) and wall-bounded turbulence research Baker & Coletti (2022). We discovered that the rotation rates of inertia-less fibers are primarily driven by turbulent fluctuations rather than mean shear. Additionally, spinning rates exceed tumbling rates Oehmke et al. (2021); Zhao et al. (2015); **?**, and the components of tumbling rates exhibit similar values in both the fiber and laboratory frames of reference.

Our method could be utilized in future research to explore the interaction between fibers and solid boundaries. Future investigations might use simultaneous measurements of curved fibers and the surrounding flow to study how near-wall structures affect the alignment of the fiber plane with the x-y plan

References

Alipour, M., De Paoli, M., Ghaemi, S., & Soldati, A. (2021). Long non-axisymmetric fibres in turbulent channel flow. *Journal of Fluid Mechanics*, *916*, A3.

Alipour, M., De Paoli, M., & Soldati, A. (2022). Influence of Reynolds number on the dynamics of rigid, slender and non-axisymmetric fibres in channel flow turbulence. *Journal of Fluid Mechanics*, *934*, A18.

Baker, L. J., & Coletti, F. (2022). Experimental investigation of inertial fibres and disks in a turbulent boundary layer. *Journal of Fluid Mechanics*, *943*, A27.

Byron, M., Einarsson, J., Gustavsson, K., Voth, G., Mehlig, B., & Variano, E. (2015). Shape-dependence of particle rotation in isotropic turbulence. *Physics of Fluids*, *27*(3).

Caridi, G. C. A., Giurgiu, V., De Paoli, M., & Soldati, A. (2023). Tracking method for curved fibres. *in preparation*.

Cleveland, W. S. (1979). Robust locally weighted regression and smoothing scatterplots. *Journal of the American statistical association*, *74*(368), 829–836.

Del Alamo, J. C., Jiménez, J., Zandonade, P., & Moser, R. D. (2004). Scaling of the energy spectra of turbulent channels. *Journal of Fluid Mechanics*, *500*, 135–144.

Elsinga, G. E., Scarano, F., Wieneke, B., & van Oudheusden, B. W. (2006). Tomographic particle image velocimetry. *Experiments in fluids*, *41*(6), 933–947.

Giurgiu, V., Caridi, G. C. A., Alipour, M., De Paoli, M., & Soldati, A. (2023). The TU Wien Turbulent Water Channel: Flow control loop and three-dimensional reconstruction of anisotropic particle dynamics. *Review of Scientific Instruments*, *94*(9).

Hoseini, A. A., Lundell, F., & Andersson, H. I. (2015). Finite-length effects on dynamical behavior of rod-like particles in wall-bounded turbulent flow. *International Journal of Multiphase Flow*, *76*, 13–21.

Kuperman, S., Sabban, L., & van Hout, R. (2019). Inertial effects on the dynamics of rigid heavy fibers in isotropic turbulence. *Physical Review Fluids*, *4*(6), 064301.

Lynch, K. M., & Park, F. C. (2017). *Modern robotics*. Cambridge University Press.

Marchioli, C., & Soldati, A. (2013). Rotation statistics of fibers in wall shear turbulence. *Acta Mechanica*, *224*, 2311–2329.

Marchioli, C., Zhao, L., & Andersson, H. (2016). On the relative rotational motion between rigid fibers and fluid in turbulent channel flow. *Physics of Fluids*, *28*(1).

Moser, R. D., Kim, J., & Mansour, N. N. (1999). Direct numerical simulation of turbulent channel flow up to $Re_\tau = 590$. *Physics of fluids*, *11*(4), 943–945.

Oehmke, T. B., Bordoloi, A. D., Variano, E., & Verhille, G. (2021). Spinning and tumbling of long fibers in isotropic turbulence. *Physical Review Fluids*, *6*(4), 044610.

Parsa, S., Calzavarini, E., Toschi, F., & Voth, G. A. (2012). Rotation rate of rods in turbulent fluid flow. *Physical review letters*, *109*(13), 134501.

Parsa, S., & Voth, G. A. (2014). Inertial range scaling in rotations of long rods in turbulence. *Physical review letters*, *112*(2), 024501.

Shaik, S., Kuperman, S., Rinsky, V., & van Hout, R. (2020). Measurements of length effects on the dynamics of rigid fibers in a turbulent channel flow. *Physical Review Fluids*, *5*(11), 114309.

Shaik, S., & van Hout, R. (2023). Kinematics of rigid fibers in a turbulent channel flow. *International Journal of Multiphase Flow*, *158*, 104262.

Voth, G. A., & Soldati, A. (2017). Anisotropic particles in turbulence. *Annual Review of Fluid Mechanics*, *49*, 249–276.

Yang, K., Zhao, L., & Andersson, H. I. (2018). Mean shear versus orientation isotropy: effects on inertialess spheroids' rotation mode in wall turbulence. *Journal of Fluid Mechanics*, *844*, 796–816.

Zhao, L., Challabotla, N. R., Andersson, H. I., & Variano, E. A. (2015). Rotation of nonspherical particles in turbulent channel flow. *Physical review letters*, *115*(24), 244501.